Southern Alaska Lithosphere and Mantle Observation Network (SALMON): A Seismic Experiment Covering the Active Arc by Road, Boat, Plane, and Helicopter

by Carl Tape, Douglas Christensen, Melissa M. Moore-Driskell, Justin Sweet, and Kyle Smith

ABSTRACT

The Southern Alaska Lithosphere and Mantle Observation Network (SALMON) is a deployment of 28 broadband, direct-burial posthole seismometers in the Cook Inlet region of the southern Alaska subduction zone. Here we describe the objectives of the project, the deployment strategy, and station design. We analyze time-dependent and frequency-dependent seismic noise for the first year of data at 18 SALMON stations, 11 of which are inside Cook Inlet basin and 7 of which are outside the basin. We compare noise at the SALMON stations with four previous collocated seismic stations, two Transportable Array stations, and one Global Seismographic Network station. The type of site, notably surface bedrock versus sedimentary basin, has the strongest impact on seismic noise levels across all periods and especially on horizontal components at long periods (> 20 s). Seismic noise and earthquakes recorded by SALMON stations reveal amplification of seismic waves in Cook Inlet basin. Aftershocks of an M_w 7.1 intraslab earthquake augment a catalog of local earthquakes to be used for source inversions and seismic imaging of the complex seismic structure in the Cook Inlet region.

Electronic Supplement: Seismic spectra, noise, seismograms, and duration estimates.

INTRODUCTION

The Southern Alaska Lithosphere and Mantle Observation Network (SALMON) is an ongoing, two-year EarthScope FlexArray project using instrumentation from the Program for the Array Seismic Studies of the Continental Lithosphere (PASSCAL). SALMON is a deployment of 28 broadband, direct-burial posthole seismometers in the Cook Inlet region of the southern Alaska subduction zone (Fig. 1). The goal of the project is to image the seismic structure of the crust and upper mantle to better understand the active tectonic setting and the tectonic history of the Cook Inlet region (Ⓔ Fig. S1, available in the electronic supplement to this article). The crust of Cook Inlet is up to 50 km thick and includes one of the largest forearc basins in the world (Clift and Vannucchi, 2004). In the lower crust beneath Cook Inlet basin is a unit that produces a magnetic-high, gravity-low signal known as the southern Alaska magnetic high (Saltus *et al.*, 1999, 2007). The source of the signal has been hypothesized to be either (1) an ancient arc accreted to the lower crust (Saltus *et al.*, 2007) or (2) serpentinized mantle (Blakely *et al.*, 2005). Seismic imaging of the lower crust of Cook Inlet has been challenging, due to inadequate station coverage, especially west of Cook Inlet, and due to the presence of the overlying sedimentary basin, which strongly amplifies seismic waves from earthquakes and from ambient noise.

Our scientific targets are active faulting, seismic structure, and mantle flow. We intend to approach these targets using techniques of moment tensor inversion, seismic imaging, and modeling of shear-wave splitting. Collaborators on the project include Stéphane Rondenay (University of Bergen), Peter Haeussler (U.S. Geological Survey [USGS] Anchorage), Paul Bedrosian (USGS Denver), and Beth Burton (USGS Denver). Rondenay used teleseismic data to image the subducting Pacific slab to the east (Rondenay *et al.*, 2008, 2010). Haeussler is part of two USGS-led projects to map the geology of the arc: (1) the Western Alaska Range project (Haeussler *et al.*, 2013) and (2) the Lake Clark/Neacola Mountains project (Todd *et al.*, 2016).

As part of the Lake Clark and Neacola Mountains project, Bedrosian and Burton led a magnetotelluric experiment at 15 sites along an arc-normal transect through Redoubt Volcano (Table 1). These magnetotelluric stations collected long-period data, sensitive to deep-crustal and upper-mantle structure, for 4–8 weeks at 12 SALMON station sites (east to west in Fig. 1: LTUX, LTUY, CLAM, KALS, HARR, HLC1–HLC5, WFLS, WFLW) and at 3 non-SALMON station sites (east

doi: 10.1785/0220160229

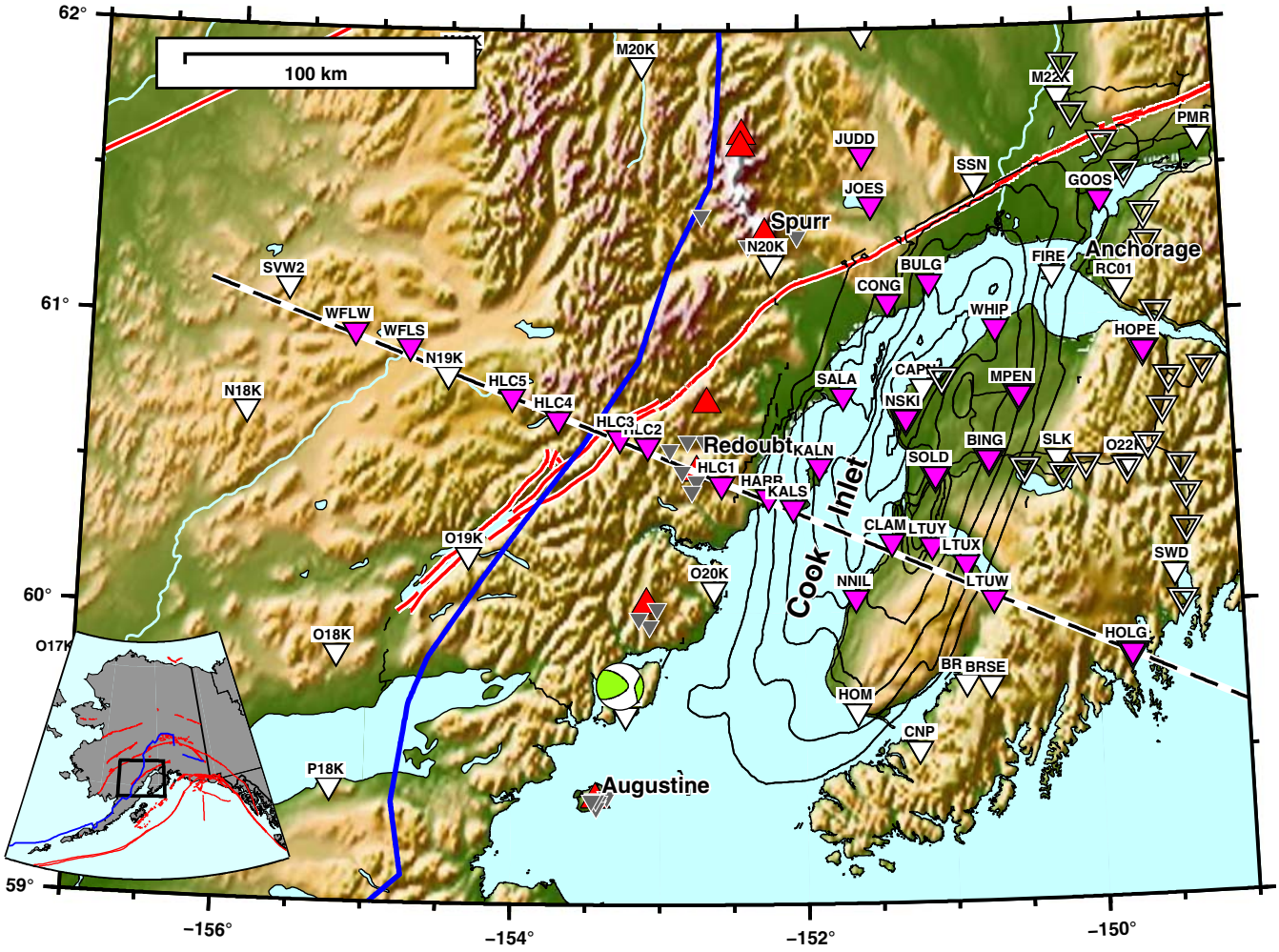

▲ **Figure 1.** Broadband stations in the Cook Inlet region, January 2017. The absence of roads west of Cook Inlet poses challenges for accessing stations. Inverted triangles denote Southern Alaska Lithosphere and Mantle Observation Network (SALMON; network ZE) stations in this study. Solid white inverted triangles denote permanent stations and stations within the temporary Transportable Array (TA). Open inverted triangles denote sites from the Multidisciplinary Observations of Onshore Subduction (MOOS) experiment from 2007 to 2009 (Abers and Christensen, 2006; Li *et al.*, 2013; Kim *et al.*, 2014). Gray inverted triangles denote intermediate-period stations from the volcanic network (AV). Active volcanoes are plotted as triangles, with labels for Augustine, Redoubt, and Spurr. The thick dashed line is the 2D target profile from Holgate glacier (HOLG) in the east, through Redoubt Volcano (elevation 3108 m), and to Sparrevohn (AT.SVW2) in the west. Contours (1 km increment) are for the Cook Inlet basin, which has a maximum depth of 7.6 km (Shellenbaum *et al.*, 2010). Active faults are plotted as thick lines (Koehler *et al.*, 2012). The thick solid line, trending approximately north–south, marks the western lateral extent of intraslab seismicity. The source mechanism is plotted for the 24 January 2016 M_w 7.1 Iniskin earthquake, which occurred within the Pacific slab at a depth of about 110 km (Ekström *et al.*, 2012). Kodiak Island, which hosts stations II.KDAK.00 and II.KDAK.10 used in our study, is just south of the region and can be seen in the inset map. The color version of this figure is available only in the electronic edition.

to west: AV.RDWB, TA.N19K, AT.SVW2). Wideband magnetotelluric data include higher frequencies and are most sensitive to upper crustal structure. These data were collected at 10 of these 15 sites, as well as at 3 new sites in the back-arc region between TA.N19K and AT.SVW2. The goal is to use the magnetotelluric data to image the subsurface structure of the subduction zone (e.g., Wannamaker *et al.*, 2014).

The SALMON experiment was the second PASSCAL experiment to use posthole sensors; the first was the Ozark, Illinois, Indiana, Kentucky (OIINK) project in the midwestern United States (Pavlis and Gilbert, 2011; Yang *et al.*, 2014), which used a combination of posthole sensors and Güralp CMG-3T sensors. We used Nanometrics Trillium T120PH posthole sensors, which are also used within the Transportable Array (TA) in Alaska (2014–2019). (The majority of the TA sensors in Alaska are STS-5A borehole sensors.) Our motivation for using posthole sensors in southern Alaska was twofold: (1) the potential for wet and tilt-prone sites and (2) challenging station access. Our scientific targets required stations in hard-to-get-to places, something that is not easily conveyed by the map in Figure 1. To our knowledge, there has not been a PASSCAL project that required the range of transportation used

Table 1
Broadband Seismic Stations in the Cook Inlet Region of Southern Alaska (Fig. 1)

Name	SALMON	Other Network	Access	MOOS	Basin Depth (km)	3D Target Region	2D Arc Profile	MT	Longitude (°)	Latitude (°)
Captain Cook		AK.CAPN	Road	YV.COOK	7.3	x	–	–	−151.01	60.79
Nikiski	**ZE.NSKI**		Road	YV.NSKI	7.0	x	–	–	−151.27	60.66
Soldotna	**ZE.SOLD**		Road	YV.SOLD	5.2	x	–	–	−151.08	60.46
Brooke Whip's place	**ZE.WHIP**		Boat (ocean)	–	5.2	x	–	–	−150.69	60.95
Beluga	ZE.BULG		Boat (ocean) + ATV	–	4.9	x	–	–	−151.09	61.12
Kalgin Island—north	**ZE.KALN**		Boat (ocean)	–	4.3	x	–	–	−151.83	60.48
Bing's Landing	**ZE.BING**		Road	YV.BING	3.7	x	–	–	−150.70	60.51
Ninilchik	**ZE.NNIL**		Road	–	3.7	x	–	–	−151.67	60.05
West Foreland	**ZE.SALA**		Boat (ocean)	–	3.7	x	–	–	−151.72	60.71
Moose Pen	ZE.MPEN		Road	YV.MPEN	3.4	x	–	–	−150.48	60.73
Congahbuna Lake	**ZE.CONG**		Boat (ocean) + ATV	–	2.7	x	–	–	−151.38	61.05
Fire Island		AK.FIRE	Helicopter	–	2.1	x	–	–	−150.22	61.14
Judd Lake	**ZE.JUDD***		Plane	–	–	x	–	–	−151.44	61.58
Joe Schuster's place	ZE.JOES		Plane	–	–	x	–	–	−151.49	61.40
Goose Bay	**ZE.GOOS***		Road	–	–	x	–	–	−149.85	61.39
Hope	**ZE.HOPE***		Road	YV.HOPE	–	x	–	–	−149.59	60.87
Cooper Landing		TA.O22K	Road	YV.SNUG	–	x	–	–	−149.74	60.47
Chisik Island		TA.O20K	Helicopter	–	–	x	-	–	−152.56	60.09
Skilak Lake		AK.SLK	Helicopter	–	–	x	–	–	−150.22	60.51
Rabbit Creek		AK.RC01	Road	–	–	x	–	–	−149.74	61.09
Susitna		AK.SSN	Helicopter	–	–	x	–	–	−150.75	61.46
Holgate glacier	ZE.HOLG		Boat (ocean)	YV.HOLG	–	x	x	–	−149.76	59.83
Lake Tustumena—east	ZE.LTUW		Boat (lake)	–	–	x	x	–	−150.70	60.03
Lake Tustumena—central	**ZE.LTUX**		Boat (lake)	–	2.4	x	x	x	−150.89	60.15
Lake Tustumena—west	**ZE.LTUY**		Boat (lake)	–	5.2	x	x	x	−151.11	60.22
Clam Gulch	**ZE.CLAM**		Road	–	4.9	x	x	x	−151.42	60.20
Kalgin Island—south	ZE.KALS		Boat (ocean)	–	3.0	x	x	x	−152.06	60.35
Harriet Point	ZE.HARR		Boat (ocean)	–	1.5	x	x	x	−152.23	60.39
Lake Clark Wilderness 1	ZE.HLC1		Helicopter	–	–	x	x	x	−152.57	60.44

The list includes SALMON stations (network ZE; Tape *et al.*, 2015) and stations in operation during the SALMON project. The 18 bold SALMON stations are featured in the noise analysis in this study. Some SALMON stations reoccupied sites from the MOOS project (2007–2009) (network YV; Abers and Christensen 2006). For basin stations, the basement depth from Shellenbaum *et al.* (2010) is listed in kilometers in parentheses. The column MT denotes sites for which long-period magnetotelluric data were collected. ATV, all-terraine vehicle; SALMON, Southern Alaska Lithosphere and Mantle Observation Network; MOOS, Multidisciplinary Observations of Onshore Subduction.
*Nonbasin SALMON station in the analysis.
(Continued next page.)

Table 1 (continued)
Broadband Seismic Stations in the Cook Inlet Region of Southern Alaska (Fig. 1)

Name	SALMON	Other Network	Access	MOOS	Basin Depth (km)	3D Target Region	2D Arc Profile	MT	Longitude (°)	Latitude (°)
Redoubt, Jurgen's Hut		AV.RDWB	Helicopter	–	–	x	x	x	−152.84	60.48
Lake Clark Wilderness 2	ZE.HLC2		Helicopter	–	–	x	x	x	−153.07	60.58
Lake Clark Wilderness 3	**ZE.HLC3***		Helicopter	–	–	–	x	x	−153.38	60.58
Lake Clark Wilderness 4	ZE.HLC4		Helicopter	–	–	–	x	x	−153.72	60.67
Lake Clark Wilderness 5	**ZE.HLC5***		Helicopter	–	–	–	x	x	−154.03	60.74
Bonanza Creek		TA.N19K	Helicopter	–	–	–	x	x	−154.51	60.82
Whitefish Lake —south	**ZE.WFLS***		Helicopter	–	–	–	x	x	−154.75	60.90
Whitefish Lake —west	**ZE.WFLW***		Helicopter	–	–	–	x	x	−155.17	60.96
Sparrevohn		AT.SVW2	Plane	–	–	–	x	x	−155.62	61.10
Total (38)	28 (18)	10		8	17	31	17	15		

The list includes SALMON stations (network ZE; Tape *et al.*, 2015) and stations in operation during the SALMON project. The 18 bold SALMON stations are featured in the noise analysis in this study. Some SALMON stations reoccupied sites from the MOOS project (2007–2009) (network YV; Abers and Christensen 2006). For basin stations, the basement depth from Shellenbaum *et al.* (2010) is listed in kilometers in parentheses. The column MT denotes sites for which long-period magnetotelluric data were collected. ATV, all-terraine vehicle; SALMON, Southern Alaska Lithosphere and Mantle Observation Network; MOOS, Multidisciplinary Observations of Onshore Subduction.
*Nonbasin SALMON station in the analysis.

within this project. Using direct-burial posthole sensors, rather than vaults with cured concrete as in previous deployments (e.g., Christensen *et al.*, 1999), our total weight and installation time were significantly reduced.

Here we document the SALMON experiment and the first year of data with two purposes in mind: (1) to explain the data quality and issues for users of the data and (2) to document the experimental design and challenges, with the potential to benefit a future experiment in this region. The network code for SALMON is ZE (Tape *et al.*, 2015). Here we will use the network label only for non-ZE-network stations, for example, TA.N19K.

EXPERIMENT DESIGN AND INSTRUMENT DEPLOYMENT

SALMON stations span two primary targets (Table 1; Fig. 1):

1. spatial coverage of the Cook Inlet basin, and
2. an arc-normal transect from Holgate glacier to Redoubt Volcano and into the back-arc region.

Cook Inlet basin is a long-lived sedimentary depocenter with distinct Mesozoic and Tertiary sections (Fisher and Magoon, 1978; Gregersen and Shellenbaum, 2016). Shellenbaum *et al.* (2010) produced a topological map of the base of the Tertiary sedimentary strata in Cook Inlet. Using this map, we classify each station as either a basin station or a nonbasin station; for each station, the base-Tertiary distance is taken to be the basement depth (Table 1). This station classification is based on Cook Inlet basin only and does not imply that all nonbasin stations are bedrock sites. For example, JOES and GOOS may be within the Beluga depocenter, southwest of Susitna basin (Saltus *et al.*, 2016).

The arc-normal transect includes both basin and nonbasin stations, as well as stations from other networks (Fig. 1). Excluding station HOLG, the distance between adjacent stations on the transect ranges from 10 km (KALS–HARR) to 40 km (CLAM–KALS), with a mean distance of 20 km.

Access to some of the remote sites was challenging. For example, Cook Inlet coastlines provided several obstacles (Fig. 2): (1) long stretches of mudflats that prevented boat landings, (2) large rocks underwater posing hazards to the boat, (3) large tides, requiring careful scheduling and limiting the amount of time at sites, and (4) high, steep bluffs with limited vegetation covering. Taking these factors into account, as well as the availability of land for permits, there were few places in Cook Inlet for seismic stations (Fig. 1). On Kenai Peninsula, access into Tustumena Lake (to LTUW, LTUX, LTUY) was only possible when the current flow out of the lake and into

▲ **Figure 2.** Access to SALMON station SALA in western Cook Inlet, showing challenging conditions. At high tide, all the rocks in view are underwater. Here a three-wheeler pulling a trailer is being driven onto the boat at a falling tide. As the boat carefully departed, its propeller was damaged on a submerged rock. Note the typical bluffs in the background; these bluffs posed challenging access to sites on top. The color version of this figure is available only in the electronic edition.

the Kasilof River was high enough. Landing a float plane in Beluga Lake (station JOES) and Judd Lake (station JUDD) required ice-free conditions, which typically occurred by mid-May.

The use of direct-burial posthole sensors allowed us to install stations that would otherwise not have been possible with a vaulted station. Previous PASSCAL projects in Alaska, notably Broadband Experiment Across the Alaska Range (BEAAR; Christensen *et al.*, 1999; Ferris *et al.*, 2003), Alaska Receiving Cross-Transects for the Inner Core (ARCTIC; Song and Christensen, 2004; Lindner *et al.*, 2010), Multidisciplinary Observations of Onshore Subduction (MOOS; Abers and Christensen, 2006; Li *et al.*, 2013), and the ongoing Wrangell Volcanic Field (WVF; Christensen and Abers, 2016) predominantly used Güralp CMG-3T sensors installed on a concrete pad about 1 m below ground level. Each installation required a wide deep hole the size of a 50-gal garbage can. A concrete pad was poured into the base of the hole and then required several hours to set. Because most of the sites were close to roads, it was possible to make multiple trips for the installations.

The direct-burial posthole sensors provided two critical advantages over the previous vault installation. First, once on site, the entire installation could be done in 60–90 min, with the variability arising from how long it takes for the the sensor mass positions to center and for the Global Positioning System (GPS) clock to lock. The short install time was essential for economic reasons at the helicopter sites because we were able to minimize the flying time and minimize the total installation time for all helicopter sites. For the boat sites in Cook Inlet, we were able to install stations during fast-changing tidal conditions; this reduced the cost of the installation by minimizing chartered-boat time. Second, the weight and volume of the installation gear were much less without the concrete mix, water, and the 50-gal can. Extra weight for the helicopter would have created additional costs beyond our budget, as well as created major challenges when scaling the bluffs in Cook Inlet.

Each of our stations was powered by six 3 volt 1200 ampere-hour Cegasa Celair air-cell batteries (Fig. 3). The batteries were housed in a partly buried 24-gal Action Packer storage container. In addition, there was a Quanterra Q330 seismic system (including digitizer), a baler for storing data, and a GPS antenna. No solar panels were used for several reasons. Given the high latitude (61°), there is relatively low radiation, which is further diminished by snow covering the panels. But the main reason is that previous deployments (Christensen *et al.*, 1999) showed that five air-cell batteries (15 V total) were needed to power a station through winter, whereas only one extra battery (18 V total) was needed to power a station for the entire year. Using solar panels with lead–acid rechargeable batteries would add a level of complexity as well as vulnerability to bear damage, while providing no financial saving. Solar panels were used for two earlier deployments in Alaska (Christensen *et al.*, 1999; Song and Christensen, 2004) but not for three recent deployments (Abers and Christensen, 2006; Tape *et al.*, 2015; Christensen and Abers, 2016).

We dug each sensor hole using a hand auger (not a two-handled posthole digger) down to a depth of about 1.2 m. The sensor manufacturer recommends a minimum depth of 1 m, noting that greater depth produces better results, with all other things being equal (Nanometrics, 2015). The choice of 1.2 m was a practical one: any deeper than this, we would not be able to reach the top of the sensor to make adjustments for orientation and leveling.

Using a wide dowel, we tamped the base of the hole, then lowered, leveled, and oriented the sensor before filling and tamping dirt on the sides of the sensor. The sensor was oriented using a Brunton compass resting on a custom aluminum pole-and-stand that slotted into the north notch in the top of the sensor. This provided a measurement precision of about 1°; however, with magnetic-based measurements, there is the possibility of systematic errors due to buried steel or ore bodies. The compass was adjusted for a declination of 16.5° for all sites. The sensor cable was buried, except for where it entered the side of the station box. A tarp, weighted with sticks or rocks,

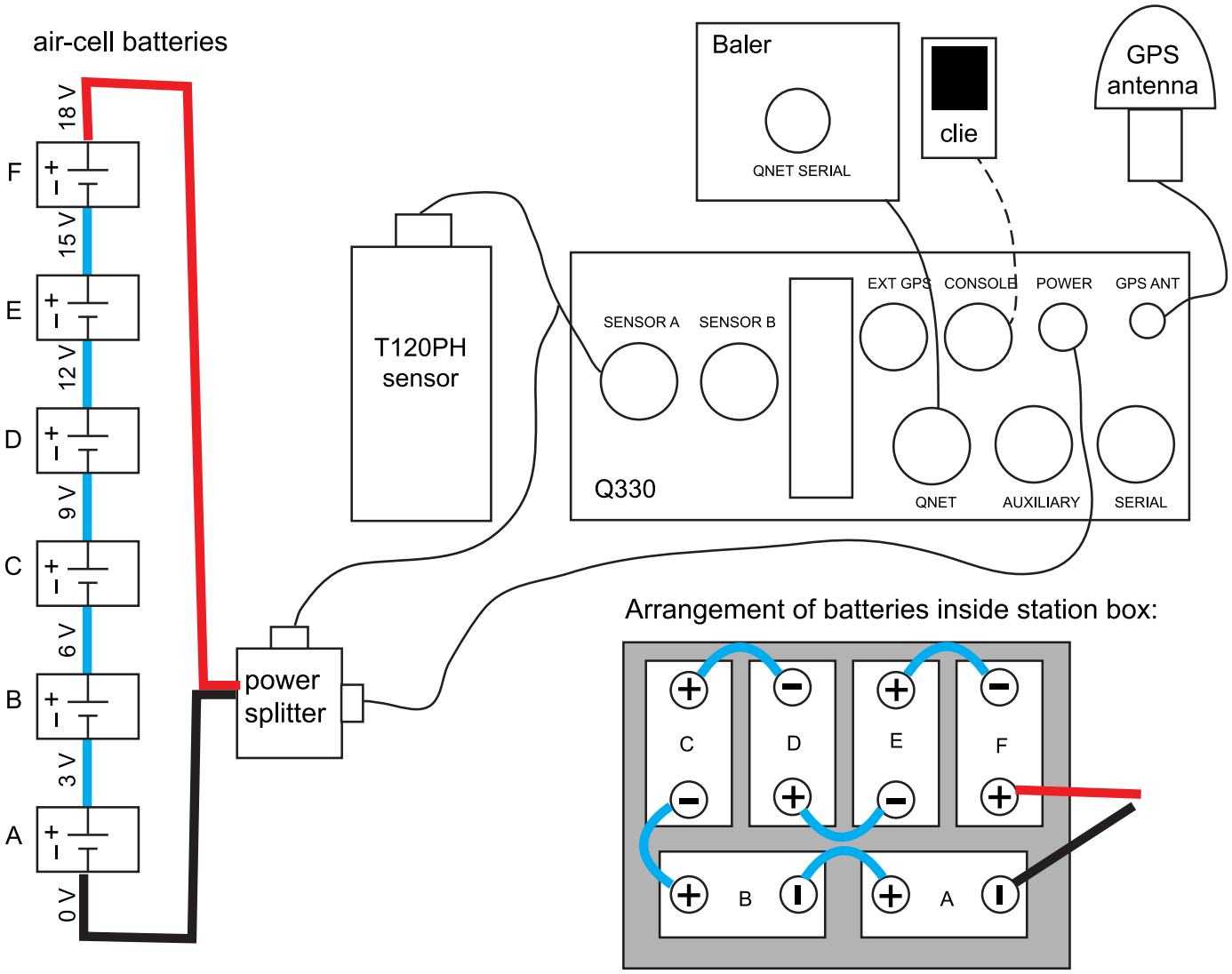

▲ **Figure 3.** Schematic setup for a SALMON seismic station. Each station contains a direct-burial posthole seismometer and partially buried box with six 3-V air-cell batteries, a Q330 digitizer, a Global Positioning System (GPS) antenna, and a baler for storing data. The color version of this figure is available only in the electronic edition.

was placed on top of the station box. A photograph of a site (HLC2) is shown in Figure 4.

Our Seymour hand auger was preferred over a Stihl power auger for several reasons. First, due to its more barbed bit, the hand auger was able to penetrate nearly frozen clay layers (at station WHIP), whereas the power auger could not. Second, it is useful even in rocky soil conditions where the power auger is unusable. Third, it felt safer in rooty soil conditions, where the power auger can abruptly get snagged, sometimes throwing the operator. Fourth, it has fewer components and is less bulky than the power auger. Fifth, it does not require fuel, which is a major benefit for transporting the auger by plane or helicopter. Finally, it is much cheaper, $50 versus several hundred dollars. We can envision few settings, such as needing hundreds of holes in ideal soil conditions, in which a power auger would save time and therefore might be preferred over a hand auger.

DATA RETURN AND DATA QUALITY (YEAR 1)

At present, we have collected the first of 2 yrs of data for the SALMON project (Tape *et al.*, 2015). Almost all of our data losses occurred at remote sites and were due to damage from bears. A total of 28 stations were installed, 15 basin stations and 13 nonbasin stations (Table 1). Among the 15 basin stations, 11 ran successfully the whole year (NSKI, SOLD, WHIP, KALN, BING, NNIL, SALA, CONG, LTUX, LTUY, CLAM), 2 died before winter due to bears (HARR, BULG), and 2 (which ran successfully) were subsequently discovered to have damaged sensors (KALS, MPEN). Among the 13 nonbasin stations, 7 ran successfully for the whole year (JUDD, GOOS, HOPE, HLC3, HLC5, WFLS, WFLW), 5 died before winter due to bears (HOLG, LTUW, HLC1, HLC2, HLC4), and 1 was installed in summer 2016 (JOES). All told, seven

▲ **Figure 4.** Example of station setup at HLC2 just west of Redoubt Volcano and adjacent to the headwaters of Drift River. Large rocks pin the tarp onto the station box, which is the only visible component of the station. Photo taken after servicing the station on 20 July 2016; view is to the west. The color version of this figure is available only in the electronic edition.

stations were disrupted by bears to the point where data stopped being recorded.

A huddle test describes the testing of a group of seismometers, all in the same location, prior to deployment in the field. During our first huddle test, with 10 sensors, the internal masses for one of the posthole sensors did not center. We shipped the sensor back to PASSCAL, who shipped it to Nanometrics, who determined that the sensor needed repairs. Apparently, the sensor was damaged in shipping from PASSCAL (located in Socorro, New Mexico) to Seward, Alaska (Ⓔ Fig. S2). In summer 2015, we collected two months of data from two road-accessible stations, BING and MPEN. Examining the MPEN data later, we discovered suspicious long-period (> 20 s) waveforms associated with earthquake waveforms. Following discussions with PASSCAL and Nanometrics, we were instructed to remove the MPEN sensor, which we were unable to do until May 2016. During station servicing in 2016, we identified similar suspicious long-period waveforms at KALS. We then plotted noise spectra from the original huddle test, and we discovered anomalously high long-period (> 20 s) noise levels on MPEN, KALS, and the sensor for which masses had not centered (Ⓔ Fig. S3). We exclude MPEN and KALS from the remaining analysis. It is likely that their waveforms are usable for arrival-time-based analyses but perhaps not for amplitude- or waveform-based analyses.

If we restrict our analysis to only the stations that survived the whole year and had no known problems (such as MPEN and KALS), then we are left with 18 stations, denoted by the bold labels in Table 1. Eleven are basin stations, and seven are nonbasin stations.

ANALYSIS OF SEISMIC NOISE

We use acceleration spectra of ambient seismic noise to examine variations among different stations. These spectra, specifically power spectral density (PSD) functions, are calculated by the Modular Utility for STAtistical kNowledge Gathering system (MUSTANG; Incorporated Research Institutions for Seismology [IRIS], 2016) using the methods of McNamara and Buland (2004). In our noise plots, for brevity, we label the y axis as Power (dB), which represents $10\log_{10}$ of the PSD relative to 1 m^{-2} s^{-4} Hz^{-1} (McNamara and Buland, 2004).

We download precomputed spectra for the time period 1 July 2015 to 31 July 2016 for vertical, east, and north components for the HH? channels. (From the Standard for Exchange of Earthquake Data (SEED) format, the HH? channels refer to a high-gain broadband seismometer with ≥ 80 samples per second.) Each spectrum spans a 1-hr time interval, with 30-min overlap of the preceding spectrum and 30-min overlap of the following spectrum (IRIS, 2016).

At each station, there is a large temporal variation in ambient noise, especially for the period of ~6 s, which is dominated by ocean-generated secondary microseism signals. We do not want to combine these variations by making an annual stack of spectra, so on the basis of seasonal noise variations (Ⓔ Fig. S4), we assign two 4-month periods of summer (June–September) and winter (November–February).

Composite spectra are useful because they tend to remove anomalous features within the individual spectra. For each station, we take the median of the hourly spectra to make a monthly spectrum. We take the mean of the four monthly spectra to make a seasonal spectrum. The composite spectra for the two horizontal components (east and north) are averaged. We also provide reference spectra for subsets of stations, such as all basin stations or nonbasin stations. These are calculated as the average of the seasonal spectra.

Figure 5 shows the summer and winter spectra for example station AK.CAPN. The seasonal difference of ~10 dB in the 2.0–10 s period range is characteristic of all stations, as shown in Ⓔ Figures S5 and S6. We provide two pairs of reference spectra within each plot. The first pair of spectra is the new high-noise model and new low-noise model of Peterson (1993). The second pair of spectra is a reference for TA for the vertical and averaged horizontal components. The steps used to make each TA spectrum are as follows (G. Sharer, e-comm., 2016): (1) Select the set of 1666 TA stations in the Lower 48 over the time period 10 May 2004 to 20 April 2015; (2) Calculate 1-hr spectra (with 30-min overlap) for each station over its lifetime, using the same methodology of McNamara and Buland (2004); (3) For one station, for each frequency, count

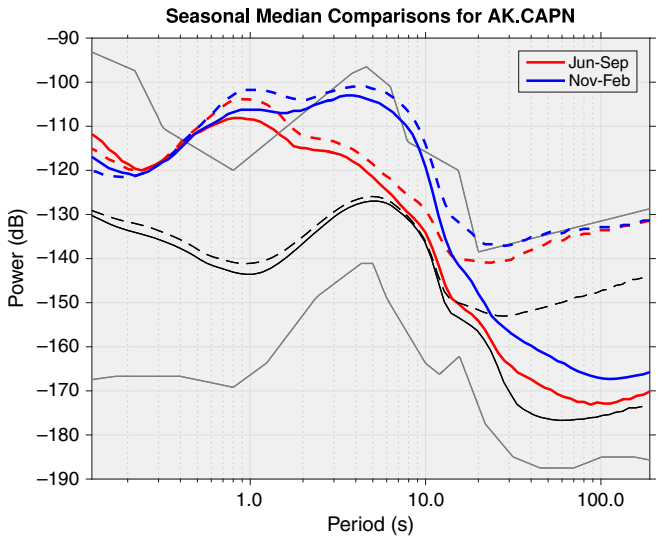

▲ **Figure 5.** Seismic noise for TA station AK.CAPN, a station overlying 7 km of sedimentary strata in Cook Inlet basin. The comparison is made for two different time periods, as identified in Ⓔ Figure S4 (available in the electronic supplement to this article): summer (June–September) and winter (November–February). The vertical component is plotted as a solid line; the average of the horizontal components is plotted as a dashed line. There are four spectra plotted for reference and used within other figures. The gray spectra are the new high-noise and low-noise models (Peterson, 1993). The black spectra are average spectra from TA sites in the Lower 48 for vertical (solid) and horizontal (dashed) components. See Ⓔ Figure S6 for plots of all 18 SALMON stations (and two TA stations) in this analysis. The color version of this figure is available only in the electronic edition.

the values in 1-dB bins to get the mode, and then make the mode spectrum; (4) Take the mean of all station lifetime mode spectra.

RESULTS

We use PSDs to examine four comparisons:

1. basin stations versus nonbasin stations,
2. TA stations versus nearby SALMON stations,
3. MOOS stations from 2007 versus SALMON stations from 2015 at the same four sites, and
4. defective sensors MPEN and KALS versus all other basin stations.

We exclude station WHIP from the interpretations below. WHIP displays no definitive problems, though we consider it to be suspicious. The site is extremely wet (in summer), which could exacerbate tilting, especially during freezing and thawing. WHIP is installed near a summer-only residence, so cultural noise (periods < 1 s) is expected to be higher during the summer. Finally, we note that WHIP was shipped in the same batch of 10 sensors that included 3 defective sensors that were presumably damaged in shipping (discussed later).

Basin Amplification of Seismic Noise

A primary focus of the SALMON project is to understand the influence of Cook Inlet basin on seismic ground motion. This influence is manifested in ambient noise, as well as in earthquake waveforms. In Figure 6a, we plot the 18 spectra for the vertical component, with each spectrum colored according to whether or not it is in the Cook Inlet basin as defined by Shellenbaum *et al.* (2010). It is clear that the basin is responsible for noise amplification at periods less than 10 s. We can make this point better by averaging the nonbasin stations (Fig. 6b) and then taking the difference between each basin-station spectrum from the nonbasin stack (Fig. 6c). Figure 7 shows the same analysis but for the horizontal component. Ⓔ Figure S10 shows a condensed perspective of Figures 6 and 7.

The residual spectra in Figures 6c and 7c provide a clear and consistent signature of the basin. Basin amplification occurs on vertical and horizontal components for periods $T \leq 10$. The largest peak occurs at periods 0.2–2.0 s (0.5–5.0 Hz), for which the difference from the nonbasin reference is up to 35 dB. The peak is the strongest for stations NSKI, KALN, and SALA, and it is the weakest for LTUX, LTUY, CONG, and BING. The spectra are labeled in order of basin thickness, ranging from 7.3 km (NSKI) to 2.4 km (LTUX) (Table 1). Although the strongest peak is at NSKI, and the weakest peak is at LTUX, in general the size of the peak does not directly relate to the thickness of the basin.

Elevated noise at basin stations is also present at long periods (> 20 s). On the vertical component, noise levels at basin stations are 5–10 dB in the winter and < 5 dB in the summer (Fig. 6c). Elevated long-period noise is stronger and more variable on the horizontal components (Fig. 7c). Tustumena Lake stations LTUX (thickness 2.4 km) and LTUY (thickness 5.2 km) appear below the nonbasin stacks, so we might conclude that basin thickness at these stations does not seem to influence the long-period noise as much as the short-period noise.

The residual spectra should be interpreted in the context of the original spectra, with an understanding of the basic features of seismic noise spectra. Global ambient noise is dominated by a broad peak known as the secondary ocean microseism (OMS) that is interpreted to originate at the seafloor from the interference of wind-generated traveling ocean waves (Longuet-Higgins, 1950; Webb, 1998; Kedar *et al.*, 2008). The secondary OMS peak is approximately twice the frequency of a much smaller primary OMS peak that arises from the interaction of traveling waves in shallow water near the coast (Hasselmann, 1963). Global analyses of seismic noise reveals strong temporal and spatial dependence of the amplitudes of the two OMS peaks (Peterson, 1993; Aster *et al.*, 2008; Stutzmann *et al.*, 2009).

For SALMON stations, the secondary OMS peak, at periods 2.0–10 s, is much clearer in the winter spectra, likely because the source of the noise is from winter storms in the northern hemisphere, including within the Gulf of Alaska (e.g., Tsai and McNamara, 2011). Within this period range, the time-dependent changes in amplitudes are similar among

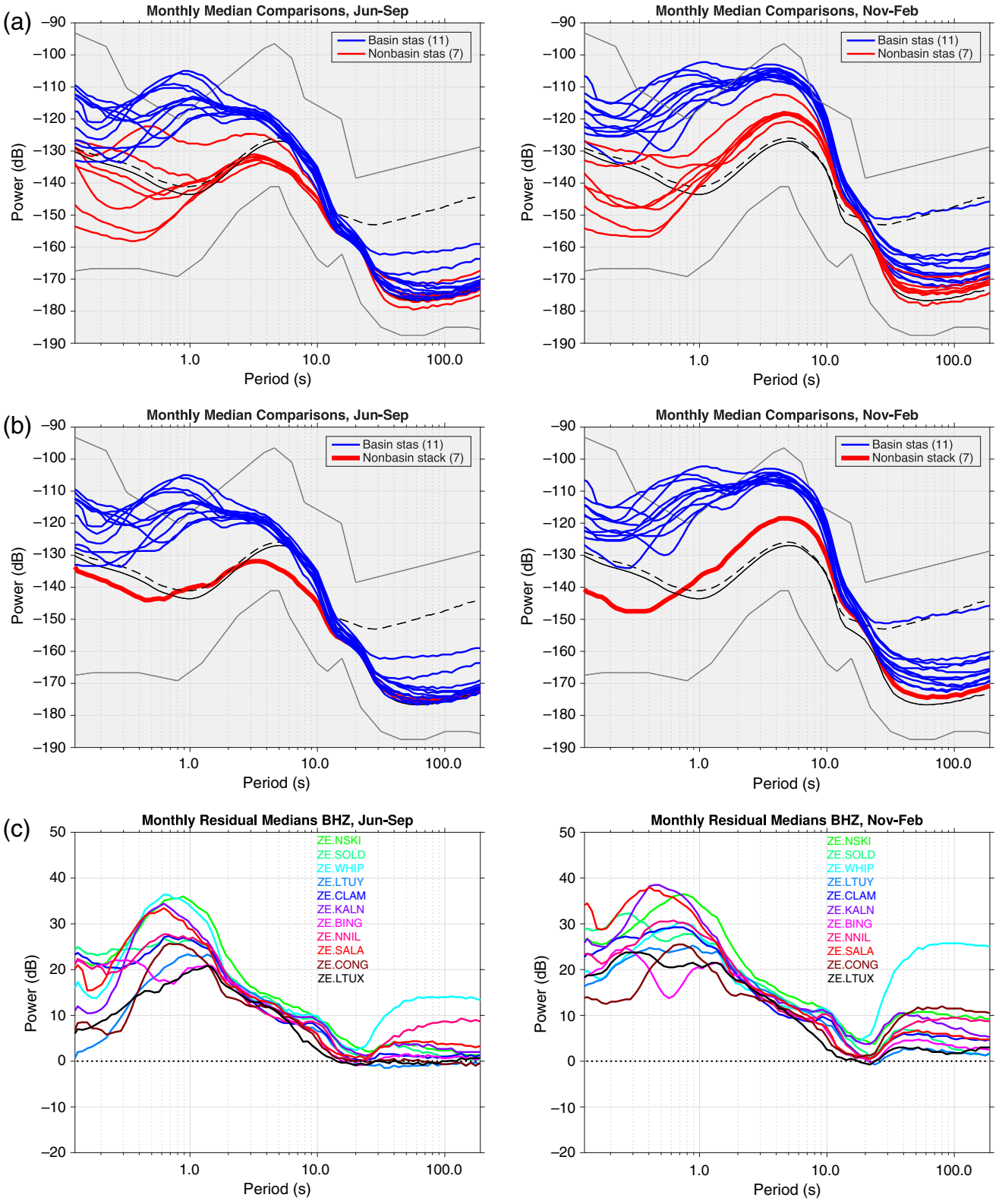

▲ **Figure 6.** Seismic noise comparison between basin sites and nonbasin sites for vertical components of ground motion. The comparison is made for two different time periods: summer (June–September), in left column, and winter (November–February), in right column. See Figure 7 for the same analysis of horizontal components. (a) Spectra for 11 basin stations and 7 nonbasin stations. (b) Same as (a), but with the nonbasin spectra collapsed into a stacked spectrum (Ⓔ Fig. S9). (c) Residual spectra between each basin station and the nonbasin stack. Almost all basin stations exhibit amplified noise across all periods for summer and winter. The color version of this figure is available only in the electronic edition.

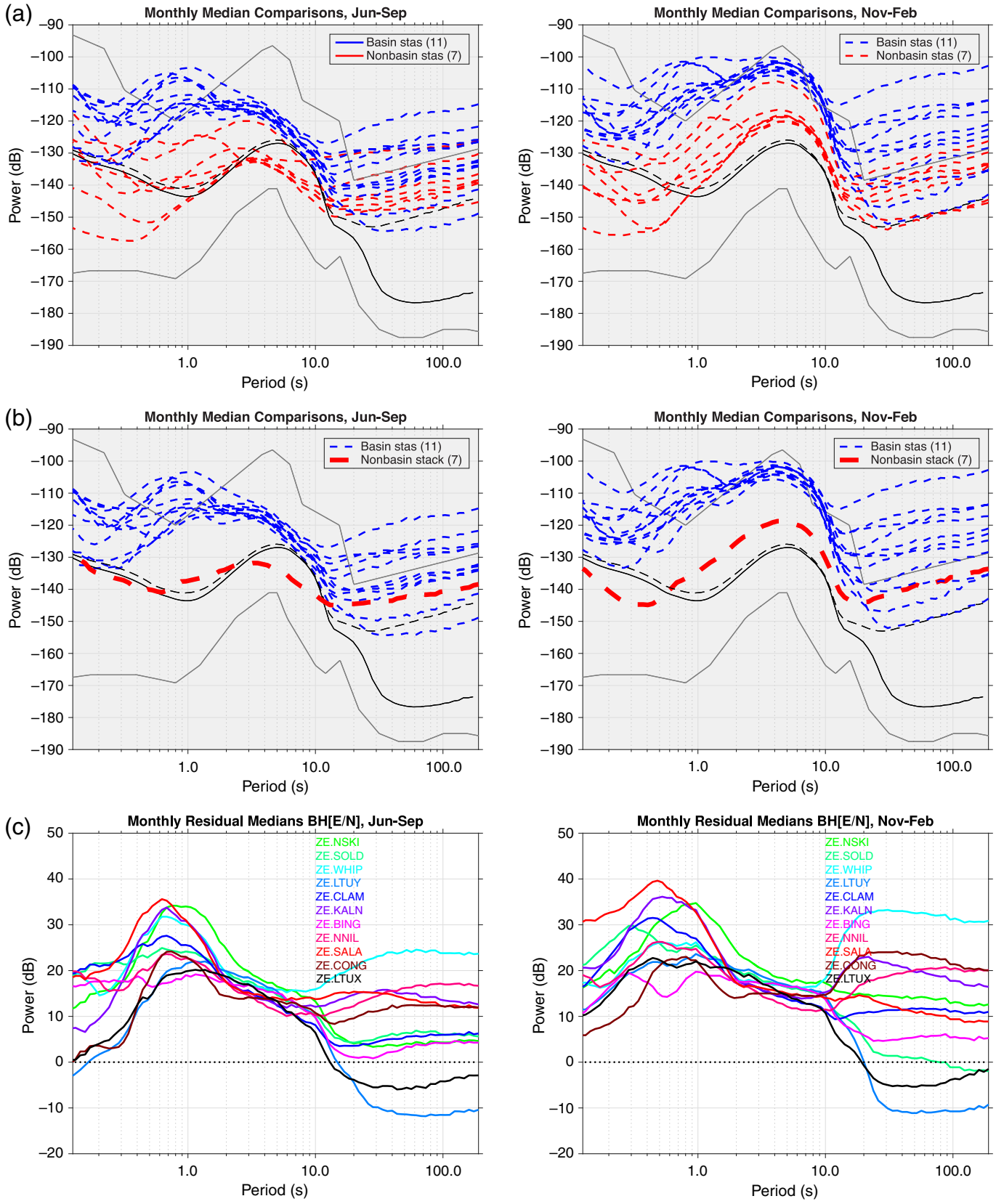

▲ **Figure 7.** Same as Figure 6, but for horizontal ground motion with two components averaged. Note the large variability in long-period (T > 10 s) amplitudes. All periods and all stations, with the exception of long periods for LTUX and LTUY (Tustumena Lake), are amplified with respect to the basin reference. The color version of this figure is available only in the electronic edition.

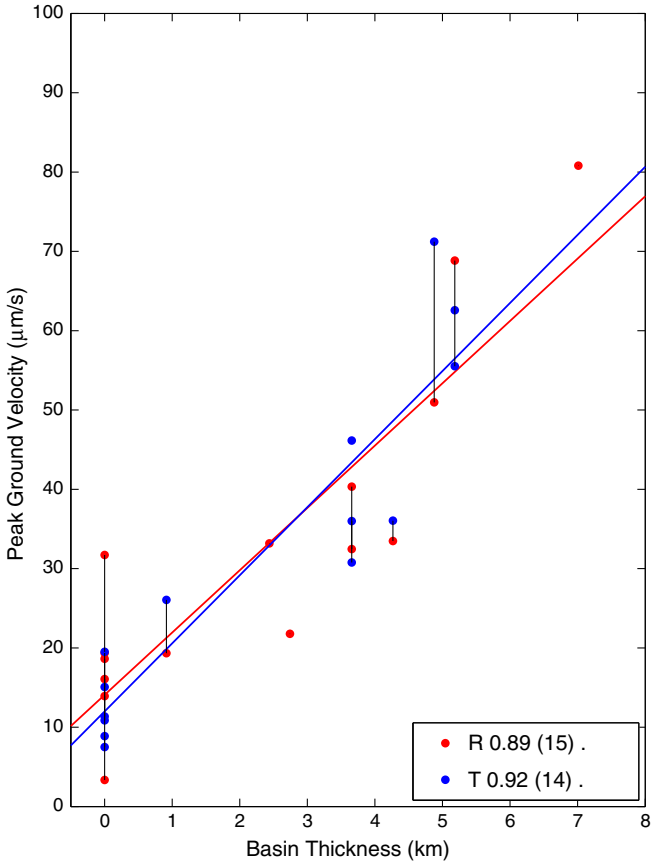

▲ **Figure 8.** The relationship between basin thickness (Shellenbaum *et al.*, 2010) and peak ground velocity (PGV) for an M_L 4.7 aftershock (24 January 2016, depth 107 km) of the M_w 7.1 Iniskin earthquake. The seismograms used to calculate PGV are band-pass filtered 1.8–4.0 s and shown in Ⓔ Figures S7 and S8. The legend shows the correlation coefficient and number of seismograms used for separate analyses of the radial component (R) and transverse component (T) seismograms. See Ⓔ Figure S11 for additional results, including shaking duration versus basin thickness. The color version of this figure is available only in the electronic edition.

all stations; Ⓔ Figure S4c shows a standard deviation of ~1 dB for the noise at a period of 6 s. The primary OMS peak is between 10 and 30 s and is most visible on the vertical components, as a shoulder of the secondary OMS (Fig. 6a).

We summarize the apparent influence of Cook Inlet basin on seismic noise by discussing patterns in period intervals marked by 0.2, 2.0, 10, and 30 s. The 0.2–2.0 s range reveals maximal noise amplification and also large variance. The 2.0–10 s range reveals amplification of 10–15 dB and low variance. The 10–30 s range differs significantly between vertical and horizontal components. On the vertical component, the primary OMS shoulder peaks are visible, and there is minimal amplification. For periods greater than 30 s, there is slightly more amplification and variance. On the horizontal components, the primary OMS shoulder peaks are not visible, and there are moderate amplification and large variance for periods greater than 10 s.

Basin Amplification from Aftershocks of an M_w 7.1 Intraslab Earthquake

On 24 January 2016, an M_w 7.1 earthquake occurred within the subducting Pacific slab at a depth of about 110 km. The Iniskin earthquake was informally named after its epicenter near Iniskin Bay. As interpreted from displacement seismograms filtered 4–80 s (Tape, 2016), most broadband stations within 250 km of the Iniskin epicenter, and especially those within Cook Inlet basin, clipped. Only four SALMON stations, all in the back-arc region and outside Cook Inlet basin, did not clip (HLC3, HLC5, WFLS, WFLW). Despite the clipping on the mainshock, we expect to have several onscale recordings of aftershocks to examine the excitation of Cook Inlet basin from intraslab earthquakes.

We calculated several metrics—duration, integrated velocity-squared, peak ground displacement, peak ground velocity (PGV), and peak ground acceleration—from band-pass-filtered seismograms for an M_L 4.7 aftershock of the Iniskin earthquake. We systematically explore different bandpasses to identify maximal correlations between basin thickness and PGV. Figure 8 shows the correlation between basin thickness and PGV for periods 1.8–4.0 s for an M_L 4.7 aftershock. With the coverage from SALMON stations inside and outside the basin, we see a clear correlation between basin thickness and the amplitude of ground motion; stations overlying the thickest sedimentary basins have the largest amplitude ground motion. For the Iniskin earthquake, the maximum damage occurred in Nikiski, where four homes burned down after a gas line ruptured, and along Kalifornsky Road near Kenai/Soldotna. The basin thicknesses at Nikiski and Kenai/Soldotna are 7.0 and 5.2 km.

Ⓔ Figure S11 provides an expanded view of Figure 8. Considering all available stations in the region, including those from TA, we see the importance of SALMON stations in investigating the influence of the basin on the duration and amplification of ground motion. We note that this analysis of amplitudes is impacted by consideration of attenuation and geometrical spreading, two factors that will depend on epicentral distance. In Ⓔ Figure S12, we show the PGV and duration values plotted as a function of epicentral distance. The lack of any trends suggests that the measured values are controlled primarily by another factor, which we show to be the basin thickness.

Comparisons between Different Sites and Different Installations

We use two TA stations, AK.CAPN and TA.N19K, for comparison with SALMON stations. Station AK.CAPN is a TA upgrade site, meaning that the site is part of a permanent network and had a functioning sensor that was upgraded with a new sensor and shallow borehole installation. The station is in Nikiski on the Kenai Peninsula at 47-m elevation. The borehole is 4.95 m deep, through sandy clay, with "Schist gravel & cobbles" at the very bottom, according to the drilling log.

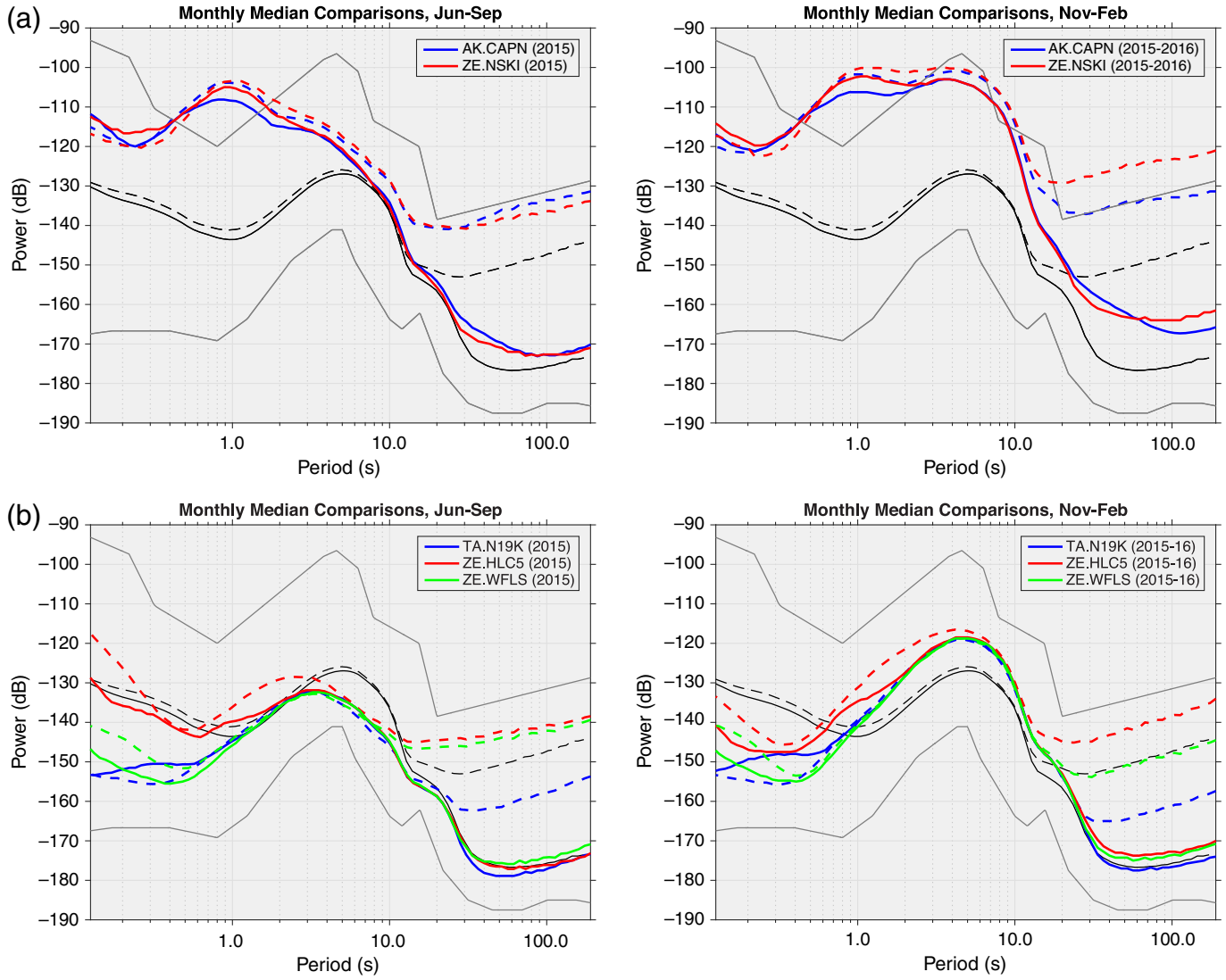

▲ **Figure 9.** Seismic noise comparison between TA sites and SALMON sites in the Cook Inlet region (Fig. 1). Solid lines are for vertical-component spectra; dashed lines are for average of horizontal components; left column is for summer; right column is for winter. (a) TA station AK.CAPN versus SALMON station NSKI. Both sites are near the deepest part of Cook Inlet basin (Table 1) and have markedly higher noise levels than the sites in (a). During the winter, the TA station AK.CAPN has 10 dB lower noise on the long-period horizontal components. (b) TA station TA.N19K versus SALMON stations HLC5 and WFLS. HLC5 and WFLS are within 30 km of TA.N19K. Compared to the SALMON sites, the TA site has significantly (15–20 dB) lower noise on the long-period horizontal components. HLC5 is noisier than WFLS (and TA.N19K) at all periods. The color version of this figure is available only in the electronic edition.

Station TA.N19K is on an unvegetated, exposed bedrock ridge at 1154-m elevation. The borehole is 2.13 m deep, with the lowermost 1 m bedrock and the overlying 1 m frost-shattered bedrock. A Nanometrics Trillium T120PH sensor is installed at the base of a grouted casing at both TA stations.

The first comparison is at the extreme basin site of Nikiski. The sites AK.CAPN and NSKI are 14 km apart and estimated to overlie 7 km of Tertiary sedimentary strata (Table 1). Both stations have Nanometrics Trillium T120PH sensors; AK.CAPN is a cased 5-m borehole, whereas NSKI is a 1.2-m direct-burial posthole. The spectra for AK.CAPN and NSKI are strikingly similar (Fig. 9a); the main discrepancy is the 10-dB lower noise level at AK.CAPN on the long-period (> 20 s) horizontal components, but only during winter.

The second comparison is from the back-arc region behind Redoubt Volcano (Fig. 1), where two SALMON sites were installed about 18 km to the west (WFLS) and 26 km to the east (HLC5) of TA station TA.N19K (Fig. 1). Spectra among the three stations are shown in Figure 9b. We first note that there are large differences even between HLC5 and WFLS; although these are both nonbasin SALMON sites, the spectra reveal large differences in the two sites. HLC5 is installed adjacent to, and possibly on top of, a glacial moraine. We suspect that the moraine is what makes HLC5 noisier than

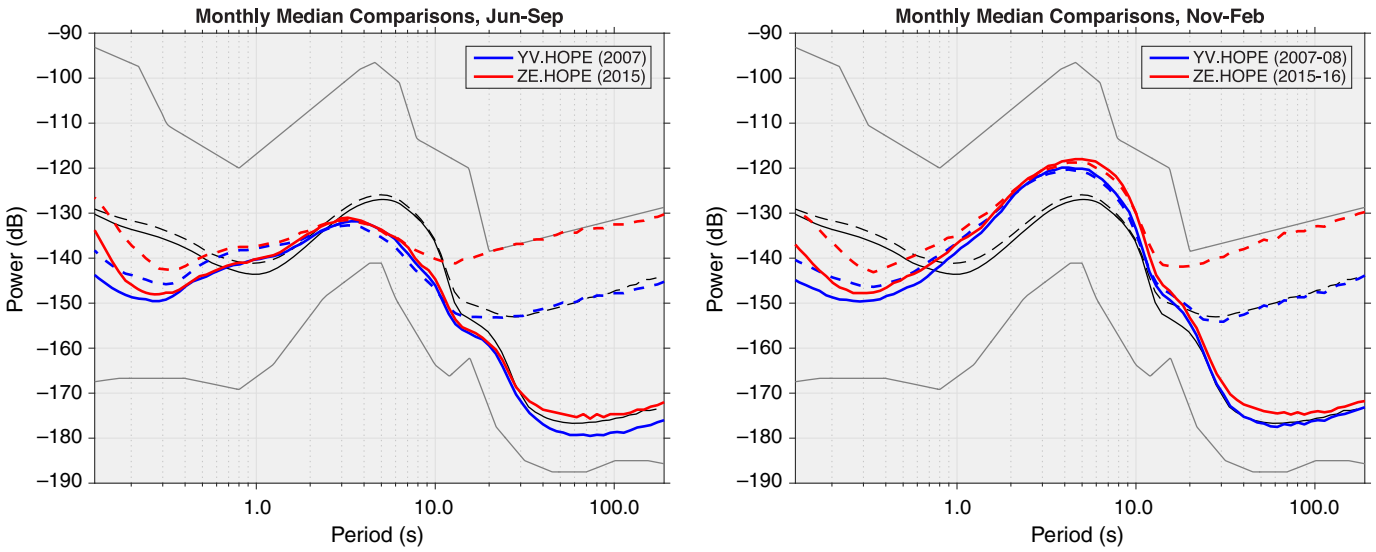

▲ **Figure 10.** Seismic noise comparison at nonbasin station HOPE from the MOOS experiment (2007–2008, network YV) and from the SALMON experiment (2015–2016, network ZE). MOOS used Güralp CMG-3T sensors in a vault, whereas SALMON used direct-burial posthole sensors (Nanometrics Trillium T120PH). Compared to the SALMON sites, the MOOS sites reveal significantly (~15 dB) lower noise on the long-period (>20 s) horizontal components (dashed lines). See Ⓔ Figure S13 for three additional stations. The color version of this figure is available only in the electronic edition.

WFLS, and we will restrict the remaining discussion to WFLS versus TA.N19K.

The spectra for WFLS are generally similar to TA.N19K, except for the long-period (>20 s) horizontals, for which TA.N19K is 10–15 dB lower. At the high frequencies (f > 1 Hz), TA.N19K has lower noise on the horizontals, whereas WFLS has lower noise on the vertical component. The differences between stations arise from differences in sites and differences in installations, which we will discuss later.

Four of the 18 SALMON stations in our analysis were installed at, or close to, previous MOOS sites. These stations allow us to compare direct-burial Trillium posthole sensors (SALMON) versus Güralp sensors installed in vaults (MOOS). Compared to the SALMON sites, the MOOS sites reveal significantly (~10 dB) lower noise on the long-period horizontal components (Fig. 10). The differences appear to be largest at the nonbasin site (HOPE) than at the basin sites (NSKI, SOLD, BING; Fig. 10). The two HOPE sites were on a steep slope and separated by 80 m, so some differences in the noise could be due to differences between the sites. Additional analysis of the regional noise at other stations operating continuously from 2007 to 2016 could help determine the extent to which the difference in the time periods (2007–2008 vs. 2015–2016) could impact our results.

Figure 11 compares spectra for the stations MPEN and KALS (both basin stations) with the average spectrum for 11 basin stations. MPEN and KALS exhibit long-period (>20 s) vertical noise levels that are 20–40 dB higher than the average basin station. For MPEN and KALS, the horizontal and vertical components of the spectra at all periods are nearly the same, indicating a problem with the sensor that was unnoticed during the huddle test but identified later after plotting spectra from the huddle-test waveforms (Ⓔ Fig. S3). Unlike with MPEN and KALS, the vertical and horizontal components for WHIP do not coincide, so we assume that local conditions are giving rise to the elevated noise levels.

DISCUSSION

Basin Amplification from Earthquakes and Noise

Using aftershocks of the M_w 7.1 Iniskin earthquake and using the Cook Inlet basement geometry (Shellenbaum *et al.*, 2010), we are able to identify correlations between basin thickness and PGV (Fig. 8) and between basin thickness and ground-motion duration (Ⓔ Fig. S11). Slow-velocity layers amplify surface waves, whereas lateral boundaries, such as with basins, trap and further amplify waves. Numerical simulations have been used to examine the influences of 1D (layers), 2D (edges), and 3D (basin shape) geometries on the amplification of surface waves (Hisada and Yamamoto, 1996; Day *et al.*, 2008; Qin *et al.*, 2012). At the simplest level, a reduction of velocities near the surface (even for a simple layered model) will lead to amplification of surface waves (Tsai and Atiganyanun, 2014).

At basin stations, amplification on the vertical and horizontal components occurs for nearly all periods but is most pronounced, and less variable, for periods less than 10 s (Figs. 6 and 7). Maximal basin amplification of 15–35 dB occurs for periods 0.2–2.0 s (0.5–5.0 Hz). During the summer months at basin stations, the noise in this period range (0.2–2.0 s) has considerably higher amplitudes than the typically dominant OMS band at 2.0–10 s (Fig. 6a).

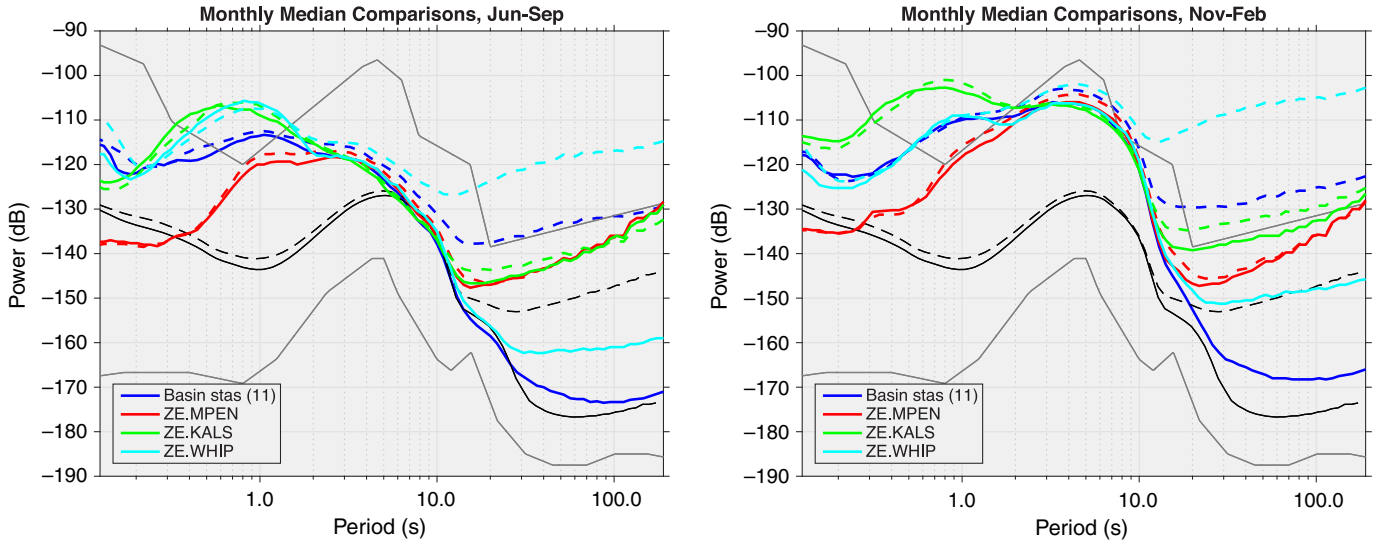

▲ **Figure 11.** Seismic noise comparison for two known defective sensors (MPEN and KALS), one high-noise station (WHIP), and a stack of 11 basin stations. The color version of this figure is available only in the electronic edition.

Long-Period Horizontal Noise Levels

Seismometers installed near the surface, especially in unconsolidated sediment, are prone to tilting, due to changes in pressure or temperature on the sensor (e.g., Sorrells 1971; Wilson *et al.*, 2002; Wolin *et al.*, 2015). This tilting can be manifested by elevated horizontal noise levels. All sensors in our analysis were installed in the uppermost 5 m, and many were installed within thick units of unconsolidated sediments. By differencing the log-scaled spectra in Ⓔ Figures S5 and S6, we produce horizontal-to-vertical (H/V) ratio spectra in Ⓔ Figures S14 and S15. The ratio spectra reveal H/V ratios of 20–50 dB for periods >20 s, and the difference between summer and winter varies between 0 and 10 dB.

Comparison between the two TA boreholes shows 20 dB lower H/V ratios for the 2-m borehole at the bedrock site (TA.N19K) than for the 5-m borehole at the extreme basin site (AK.CAPN). Although it is tempting to propose that the structure at the site may govern the H/V ratio, we do not see a clear pattern of enhanced H/V ratios for basin stations when we examine the 18 SALMON station (Ⓔ Fig. S15).

Anthony *et al.* (2015) showed that H/V ratio spectra for shallow vault sites in Antarctica revealed elevated ratios for long periods (with the same pattern as in our Ⓔ Fig. S15), whereas H/V spectra from deep (>100 m) borehole sites did not. They suggest that the elevated H/V ratios are caused by seismometer tilting, with the implication that a >100 m borehole could remove the unwanted signal.

To examine the influence of a deeper borehole on the noise in southern Alaska, we analyze the closest Global Seismographic Network (GSN) station, which is about 300 km south of the SALMON stations, on Kodiak Island. This site hosts two sensors: (1) II.KDAK.00, a Geotech KS-54000 sensor installed at 88-m depth within a cased borehole in fractured bedrock, and (2) II.KDAK.10, a Nanometrics Trillium T120PH sensor installed at 5-m depth within a cased borehole in fractured bedrock. Both II.KDAK sensors exhibit the lowest long-period (>20 s) noise levels of any stations in our analysis (Ⓔ Fig. S5). Yet neither sensor, and notably the one at 88-m depth, exhibits near-zero H/V ratio spectra (Ⓔ Fig. S14). The station with the lowest horizontal noise levels, II.KDAK.10, is also the station with the lowest H/V ratio, which is 10–15 dB for periods >40 s. The borehole sensor (II.KDAK.00) has a known issue on a horizontal component that could be the source of the higher-than-expected horizontal noise level and H/V ratio (P. Davis, e-comm., 2017).

Susceptibility of basin sites to tilting could explain some of the large variability in the spectra for horizontal components (Fig. 7c). It is unclear whether this could also explain, for example, the 0–10 dB elevated noise levels on the vertical component of basin stations (Fig. 6c). Understanding the influence of the basin on long-period noise levels is complicated, because we have seen that low-velocity layers near the surface can amplify seismic waves and also enhance tilting of the sensor from thermal and pressure effects.

Influence of Site and Installation

Ideally, a comparison between two stations would be made over the same time period and at the same site, with only one factor, for example, sensor or installation style, would differ. For example, at the quiet test site at Poker Flat in central Alaska, Sweet *et al.* (2015) found that a shallowly buried Nanometrics Trillium T120PH exhibited long-period horizontal components that were 5–10 dB quieter than those from a collocated, simultaneously recording Trillium 120PA in a shallowly buried vault. In our study, we are attempting to isolate factors, such as site or installation, in less-than-ideal scenarios, whereby a single factor cannot be isolated.

Comparison between four SALMON stations (one nonbasin and three basin) and four collocated MOOS stations from 2007 to 2008 indicates that the combination of a vault and Güralp CMG-3T sensor produces lower horizontal noise levels than the direct-burial Nanometrics Trillium T120PH posthole sensor. Because the ambient noise levels of the spectra are above the sensor self-noise levels for the Nanometrics Trillium T120PH (SALMON) and Güralp CMG-3T (MOOS) sensors (Ringler and Hutt, 2010), we attribute the differences in spectra to installation, not to the sensor.

Comparisons between TA stations and SALMON stations (Fig. 9) reveal advantages of both site selection and installation for the TA stations. In the back-arc region, the bedrock site at TA.N19K produces lower horizontal noise levels than the nonbasin site WFLS. In the deepest basin region near Nikiski, the 5-m borehole at AK.CAPN exhibited 10 dB lower noise levels on long-period (> 20 s) horizontal components but only during winter. Because the sites at AK.CAPN and NSKI were similar (though separated by 14 km), we attribute the reduced noise levels to the deeper (and cased) borehole.

SUMMARY

After one year of the project, we can offer some insights on deployment strategies in the Cook Inlet region of southern Alaska:

1. Access to remote sites, by which we mean sites inaccessible by road, is challenging. Helicopter or, if possible, float planes are needed north of Cook Inlet. River boats are needed to access the three sites on Tustumena Lake (Fig. 1), and ocean boats are needed to access the site near Holgate glacier and the sites in Cook Inlet (Fig. 1). Given the bluffs, mud flats, rocky shores, and tides in Cook Inlet, there are few viable sites for stations.
2. Some ground may be too frozen to dig in May, as we discovered at BING.
3. Traditional vault installations (e.g., Christensen *et al.*, 1999) require heavier loads and longer wait times than direct-burial posthole installations. The ease of installation (≤ 1.5 hrs) for the posthole sensors allowed us to reach boat-chartered and helicopter-chartered sites within the constraints of our budget. Heavier loads (e.g., for concrete) or longer wait times (e.g., for concrete to set) would not have been feasible without a much larger budget.
4. Bears were the only cause of data loss, excluding two defective sensors (MPEN, KALS). Bear disturbances occurred exclusively at remote sites. Our investigation of bear disturbances is ongoing and being done in conjunction with a second temporary deployment, in central Alaska (Tape and West, 2014).
5. Our power system of 18-V of air-cell batteries (Fig. 3) worked for the full year in all cases except one: the defective station MPEN ran out of power after 11 months.
6. It is critical to perform huddle tests and carefully analyze the data, both in the time domain and in the frequency domain, because this can reveal sensor problems (Ⓔ Fig. S3). Having other personnel, such as PASSCAL technicians, examine the data prior to deployment is prudent.

We analyze time-dependent and frequency-dependent seismic noise for 18 SALMON stations for the first year of data. Variations in seismic noise provide useful diagnostics for station quality and site conditions. Our main points are as follows:

1. Seismic noise at periods 2.0–30 s is 5–15 dB greater during winter than during summer. This is a regional signature that arises from stronger ocean-generating microseisms in the (northern hemisphere) winter.
   Given the strong seasonal differences across all periods (Fig. 5 and Ⓔ Figs. S5 and S6), we provide all comparisons for two 4-month time periods: summer (June–September) and winter (November–February).
2. Differences among sites accounted for the largest variations in seismic noise for the 0.2–2.0 s period range. Basin stations (Table 1; Fig. 1) exhibited 20–35 dB higher noise levels on vertical and horizontal components (Figs. 6 and 7). Within the 2.0–10 s period range of secondary OMSs, noise levels were 10–15 dB higher on basin stations.
   Basin stations have noise spectra for which the highest amplitude peak (0.2–2.0 s) is as large as or greater than the typically dominant secondary OMS peak (2.0–10 s) (Fig. 5).
3. Examining an M_w 4.7 aftershock of the M_w 7.1 Iniskin earthquake, we find a correlation between basin depth and PGV for the 1.8–4.0 s period range (Fig. 8).
   The seismic noise over this period range is amplified by 10–15 dB at basin stations (Figs. 6 and 7).
4. All stations in the analysis, including two TA stations in shallow boreholes and two GSN sensors in shallow and deep boreholes, exhibit enhanced H/V noise levels at periods > 20 s. The implication from high-quality installations at TA.N19K (2-m borehole in bedrock), AK.CAPN (5-m borehole in sediments), II.KDAK.10 (5.5-m borehole in bedrock), and II.KDAK.00 (88 m in bedrock), in comparison with SALMON sites, suggests that the selection of site is the most important factor for reducing noise levels. The TA and GSN are capable of drilling into bedrock and can therefore use bedrock sites. The next important factor is to put the seismometer deep below the surface (Hutt *et al.*, 2017). Relative to the direct-burial approach, the shallow (2–5 m) cased borehole reduces noise levels on the long-period horizontal components. A deep (~100 m) borehole might be expected to further reduce the horizontal noise levels and amplified H/V ratios, but we did not see this for station II.KDAK.00 at Kodiak.
5. Comparison between four collocated stations from SALMON (2015–2016) and MOOS (2007–2008) reveal lower long-period horizontal noise levels on the Güralp CMG-3T vault installations than for the Nanometrics Trillium T120PH direct-burial posthole installations (Fig. 10). Further experiments dedicated to seismometer

testing are needed to reduce the variables within such comparisons.

We provided an assessment of data quality that may be useful to future users of SALMON seismic data. Our analysis of seismic noise follows a tradition of examining variations in long-period (> 20 s) horizontal noise levels, which can exhibit variations that are not due to ground motion (e.g., Wilson *et al.*, 2002; Aderhold *et al.*, 2015; Anthony *et al.*, 2015; Wolin *et al.*, 2015). The relevance of long-period horizontal noise, or the consequence of high noise, will depend on the user of the data. In some cases, such as seismic-wave amplification due to Cook Inlet basin, high noise levels are precisely what we are expecting. The high-noise basin stations provide the only means for modeling the complex, high-amplitude seismic waveforms that arise from the structural complexity of the basin. For local earthquake studies using arrival times (seismicity patterns, first-motion focal mechanism, ray-based seismic imaging) the elevated levels of long-period horizontal noise are not expected to pose a significant issue. For local earthquake studies using three-component waveforms (moment tensor inversion, waveform-based tomography, periods 2–40 s), the elevated noise will pose challenges similar to those faced in other active tectonic settings with sedimentary basins (e.g., Liu *et al.*, 2004; Tape *et al.*, 2009).

We look forward to using intraslab and crustal earthquakes, recorded from summer 2015 to summer 2017, to seismically image the complex crustal structure and uppermost mantle structure in the Cook Inlet region. A detailed reliable seismic velocity model would be valuable for interpreting the tectonic history of the region.

DATA AND RESOURCES

Seismic noise power spectral densities (PSDs) and seismic waveforms for the Southern Alaska Lithosphere and Mantle Observation Network (SALMON) project (network ZE, Tape *et al.*, 2015, doi: 10.7914/SN/ZE_2015) are archived at the Incorporated Research Institutions for Seismology (IRIS) Data Management Center (DMC). Noise PSDs are openly available; waveforms will be available, unrestricted, starting August 2019. All other seismic waveforms used in this study (TA.N19K, AK.CAPN, II.KDAK) are available at the IRIS-DMC. A list of active volcanoes (e.g., Fig. 1) was downloaded from the Alaska Volcano Observatory webpage at https://avo.alaska.edu/volcanoes/latlong.php (last accessed November 2016).

ACKNOWLEDGMENTS

We thank Southern Alaska Lithosphere and Mantle Observation Network (SALMON) field assistants for their efforts in deploying and servicing stations: Amanda McPherson, Nealey Sims, Kyle Smith, Kathleen McKee, Martin Harrild, Paul Bedrosian, and Beth Burton. The University of Alaska Fairbanks (UAF) Marine Science Center in Seward provided space for storing, shipping, and testing seismic equipment. The Program for the Array Seismic Studies of the Continental Lithosphere (PASSCAL) provided training, equipment, and consulting support for the seismic deployment. PASSCAL and the Incorporated Research Institutions for Seismology (IRIS) Data Management Center (DMC) provided support in archiving and distributing the seismic waveforms from the project. Erin Todd and Jamey Jones of the U.S. Geological Survey (USGS) Alaska Science Center provided logistical support for the helicopter deployment of stations in the Lake Clark region. Our noise spectra plots were generated using a code originally written by Andy Frassetto. Bob Busby provided the drilling logs for TA.N19K and AK.CAPN; Pete Davis provided the drilling log for II.KDAK.00. The SALMON FlexArray EarthScope project is supported by National Science Foundation (NSF) Grant EAR 1251971. This article benefited from two reviews (Kasey Aderhold and an anonymous reviewer) and from feedback from Noel Barstow, Bob Busby, Peter Haeussler, and Adam Ringler.

REFERENCES

Abers, G., and D. Christensen (2006). *Seismic and Geodetic Imaging of Subducting Terranes under North America*, International Federation of Digital Seismograph Networks, Other/Seismic Network, doi: 10.7914/SN/YV_2006.

Aderhold, K., K. E. Anderson, A. M. Reusch, M. C. Pfeifer, R. C. Aster, and T. Parker (2015). Data quality of collocated portable broadband seismometers using direct burial and vault emplacement, *Bull. Seismol. Soc. Am.* **105,** no. 5, 2420–2432, doi: 10.1785/0120140352.

Anthony, R. E., R. C. Aster, D. Wiens, A. Nyblade, S. Anandakrishnan, A. Huerta, J. P. Winberry, T. Wilson, and C. Rowe (2015). The seismic noise environment of Antarctica, *Seismol. Res. Lett.* **86,** no. 1, 89–100, doi: 10.1785/0220140109.

Aster, R. C., D. E. McNamara, and P. D. Bromirski (2008). Multidecadal climate-induced variability in microseisms, *Seismol. Res. Lett.* **79,** no. 2, 194–202, doi: 10.1785/gssrl.79.2.194.

Blakely, R. J., T. M. Brocher, and R. E. Wells (2005). Subduction-zone magnetic anomalies and implications for hydrated forearc mantle, *Geology* **33,** no. 6, 445–448.

Christensen, D., and G. Abers (2016). *Fate and consequences of Yakutat terrane subduction beneath eastern Alaska and the Wrangell Volcanic Field*, International Federation of Digital Seismograph Networks, Other/Seismic Network, doi: 10.7914/SN/YG_2016.

Christensen, D., G. Abers, and R. Hansen (1999). *Broadband Experiment Across Alaskan Range*, International Federation of Digital Seismograph Networks, Other/Seismic Network, doi: 10.7914/SN/XE_1999.

Clift, P., and P. Vannucchi (2004). Controls on tectonic accretion versus erosion in subduction zones: Implications for the origin and recycling of the continental crust, *Rev. Geophys.* **42,** no. RG2001, doi: 10.1029/2003RG000127..

Day, S. M., R. Graves, J. Bielak, D. Dreger, S. Larsen, K. B. Olsen, A. Pitarka, and L. Ramierez-Guzman (2008). Model for basin effects on long-period response spectra in southern California, *Earthq. Spectra* **24,** no. 1, 257–277.

Ekström, G., M. Nettles, and A. M. Dziewoński (2012). The global CMT project 2004–2010: Centroid-moment tensors for 13,017 earthquakes, *Phys. Earth Planet. In.* **200/201,** 1–9, doi: 10.1016/j.pepi.2012.04.002.

Ferris, A., G. A. Abers, D. H. Christensen, and E. Veenstra (2003). High resolution image of the subducted Pacific (?) plate beneath central

Alaska, 50–150 km depth, *Earth Planet. Sci. Lett.* **214,** nos. 3/4, 575–588.
Fisher, M. A., and L. B. Magoon (1978). Geologic framework of lower Cook Inlet, Alaska, *Am. Assoc. Petrol. Geol. Bull.* **62,** no. 3, 373–402.
Gregersen, L. S., and D. P. Shellenbaum (2016). Top Mesozoic unconformity subcrop map, Cook Inlet basin, Alaska, *Alaska Div. Geol. Geophys. Surv. Rept. of Investigation 2016-4*, 1 sheet, scale 1:500,000, available at http://www.dggs.alaska.gov/pubs/id/29658 (last accessed November 2016).
Haeussler, P. J., D. Bradley, P. W. Layer, R. M. Friedman, P. O'sullivan, J. V. Jones III, S. M. Karl, S. E. Box, and E. Todd (2013). Magmatic history of the Tordrillo Mountains and Western Alaska Range and tectonic implications, *Geol. Soc. Am. Abstr. Progr.* 45**,** 77.
Hasselmann, K. (1963). A statistical analysis of the generation of microseisms, *Rev. Geophys.* **1,** no. 2, 177–210.
Hisada, Y., and S. Yamamoto (1996). One-, two-, and three-dimensional site effects in sediment-filled basins, *Proc. of the 11th World Conf. on Earthquake Engineering*, Paper No. 2040.
Hutt, C. R., A. T. Ringler, and L. S. Gee (2017). Broadband seismic noise attenuation versus depth at the Albuquerque Seismological Laboratory, *Bull. Seismol. Soc. Am.* **107,** no. 3, doi: 10.1785/0120160187.
Incorporated Research Institutions for Seismology (IRIS) (2016). IRIS DMC Web Services, *Services Implementation: MUSTANG*, available at http://service.iris.edu/mustang/ (last accessed November 2016).
Kedar, S., M. Longuet-Higgins, F. Webb, N. Graham, R. Clayton, and C. Jones (2008). The origin of deep ocean microseisms in the North Atlantic Ocean, *Proc. Math. Phys. Eng. Sci.* **464,** 777–793, doi: 10.1098/rspa.2007.0277.
Kim, Y., G. A. Abers, J. Li, D. Christensen, J. Calkins, and S. Rondenay (2014). Alaska Megathrust 2: Imaging the megathrust zone and Yakutat/Pacific plate interface in the Alaska subduction zone, *J. Geophys. Res.* **119,** 1924–1941, doi: 10.1002/2013JB010581.
Koehler, R. D., R.-E. Farrell, P. A. C. Burns, and R. A. Combelick (2012). Quaternary faults and folds in Alaska: A digital database, *Miscellaneous Publication 141*, Alaska Division of Geological & Geophysical Surveys, Fairbanks, Alaska, 31 pp., 1 sheet, scale 1:3,700,000.
Li, J., G. A. Abers, Y. Kim, and D. Christensen (2013). Alaska megathrust 1: Seismicity 43 years after the great 1964 Alaska megathrust earthquake, *J. Geophys. Res.* **118,** 4861–4871, doi: 10.1002/jgrb.50358.
Lindner, D., X. Song, P. Ma, and D. H. Christensen (2010). Inner core rotation and its variability from nonparametric modeling, *J. Geophys. Res.* **115,** no. B04307, doi: 10.1029/2009JB006294.
Liu, Q., J. Polet, D. Komatitsch, and J. Tromp (2004). Spectral-element moment tensor inversions for earthquakes in southern California, *Bull. Seismol. Soc. Am.* **94,** no. 5, 1748–1761, doi: 10.1785/012004038.
Longuet-Higgins, M. S. (1950). A theory of the origin of microseisms, *Phil. Trans. Roy. Soc. Lond. A* **243,** 1–35.
McNamara, D. E., and R. P. Buland (2004). Ambient noise levels in the continental United States, *Bull. Seismol. Soc. Am.* **94,** no. 4, 1517–1527, doi: 10.1785/012003001.
Nanometrics (2015). Trillium Posthole User Guide, *Part Number 17217R6*, 59 pp.
Pavlis, G., and H. Gilbert (2011). *Ozark Illinois Indiana Kentucky (OIINK) Flexible Array Experiment*, International Federation of Digital Seismograph Networks, Other/Seismic Network, doi: 10.7914/SN/XO_2011.
Peterson, J. (1993). Observations and modeling of seismic background noise, *U.S. Geol. Surv. Open-File Rept. 93-322*.
Qin, Y., Y. Wang, H. Takenaka, and X. Zhang (2012). Seismic ground motion amplification in a 3D sedimentary basin: The effect of the vertical velocity gradient, *J. Geophys. Eng.* **9,** no. 6, 761–772, doi: 10.1088/1742-2132/9/6/761.
Ringler, A. T., and C. R. Hutt (2010). Self-noise models of seismic instruments, *Seismol. Res. Lett.* **81,** no. 6, 972–983, doi: 10.1785/gssrl.81.6.972.
Rondenay, S., G. A. Abers, and P. E. van Keken (2008). Seismic imaging of subduction zone metamorphism, *Geology* **36,** no. 4, 275–278.
Rondenay, S., L. G. J. Montési, and G. A. Abers (2010). New geophysical insight into the origin of the Denali volcanic gap, *Geophys. J. Int.* **182,** 613–630.
Saltus, R. W., T. L. Hudson, and G. G. Connard (1999). A new magnetic view of Alaska, *GSA Today* **9,** no. 3, 1–6.
Saltus, R. W., T. L. Hudson, and F. H. Wilson (2007). The geophysical character of southern Alaska—Implications for crustal evolution, in *Tectonic Growth of a Collisional Continental Margin: Crustal Evolution of Southern Alaska, USA*, K. D. Ridgway, J. M. Trop, J. M. G. Glen, and J. M. O'Neill (Editors), Geol. Soc. Am. Spec. Pap. 431, Boulder, Colorado, 1–20.
Saltus, R. W., R. G. Stanley, P. J. Haeussler, J. V. Jones III, C. J. Potter, and K. A. Lewis (2016). Late Oligocene to present contractional structure in and around the Susitna basin, Alaska—Geophysical evidence and geological implications, *Geosphere* **12,** no. 5, 1378–1390, doi: 10.1130/GES01279.1.
Shellenbaum, D. P., L. S. Gregersen, and P. R. Delaney (2010). Top Mesozoic unconformity depth map of the Cook Inlet Basin, Alaska, *Alaska Div. Geol. Geophys. Surv. Rept. of Investigation 2010-2*, 1 sheet, scale 1:500,000, available at http://www.dggs.alaska.gov/pubs/id/21961 (last accessed November 2016).
Song, X., and D. Christensen (2004). *CSEDI: Observational and Theoretical Constraints on the Structure and Rotation of the Inner Core*, International Federation of Digital Seismograph Networks, Other/Seismic Network, doi: 10.7914/SN/XR_2004.
Sorrells, G. G. (1971). A preliminary investigation into the relationship between long-period seismic noise and local fluctuations in the atmospheric pressure field, *Geophys. J. Roy. Astron. Soc.* **26,** 71–82.
Stutzmann, E., M. Schimmel, G. Patau, and A. Maggi (2009). Global climate imprint on seismic noise, *Geochem. Geophy. Geosys.* **10,** no. 11, doi: 10.1029/2009GC002619.
Sweet, J., B. Beaudoin, N. Barstow, C. Pfeifer, A. Frassetto, and K. Anderson (2015). Posthole broadband sensor emplacement vs. surface vaults: Observations of comparative noise performance and tradeoffs, presented at *2015 Fall Meeting, AGU*, San Francisco, California, 14–18 December, Abstract S33D–2802.
Tape, C. (2016). *Analysis of Regional Seismograms and 3D Synthetic Seismograms for the 2016-01-24 Mw 7.1 Iniskin Earthquake in Southern Alaska*, available at http://hdl.handle.net/11122/6983 (last accessed November 2016).
Tape, C., and M. E. West (2014). *Fault Locations and Alaska Tectonics from Seismicity*, International Federation of Digital Seismograph Networks, Other/Seismic Network, doi: 10.7914/SN/XV_2014.
Tape, C., D. H. Christensen, and M. M. Driskell (2015). *Southern Alaska Lithosphere and Mantle Observation Network*, International Federation of Digital Seismograph Networks, Other/Seismic Network, doi: 10.7914/SN/ZE_2015.
Tape, C., Q. Liu, A. Maggi, and J. Tromp (2009). Adjoint tomography of the southern California crust, *Science* **325,** 988–992, doi: 10.1126/science.1175298.
Todd, E., J. V. Jones III, and A. Kylander-Clark (2016). Zircon ages and compositions constrain the nature and sources of melting during and after progressive accretion of the Wrangellia Composite Terrane to the southern Alaska margin, presented at the *Goldschmidt Meeting*, Yokohama, Japan, 26 June–1 July, Abstract.
Tsai, V. C., and S. Atiganyanun (2014). Green's functions for surface waves in a generic velocity structure, *Bull. Seismol. Soc. Am.* **104,** no. 5, 2573–2578, doi: 10.1785/0120140121.

Tsai, V. C., and D. E. McNamara (2011). Quantifying the influence of sea ice on ocean microseism using observations from the Bering Sea, Alaska, *Geophys. Res. Lett.* **38,** L22502, doi: 10.1029/2011GL049791.

Wannamaker, P. E., R. L. Evans, P. A. Bedrosian, M. J. Unsworth, V. Maris, and R. S. McGary (2014). Segmentation of plate coupling, fate of subduction fluids, and modes of arc magmatism in Cascadia, inferred from magnetotelluric resistivity, *Geochem. Geophy. Geosys.* **15,** 4230–4253, doi: 10.1002/2014GC005509.

Webb, S. C. (1998). Broadband seismology and noise under the ocean, *Rev. Geophys.* **36,** no. 1, 105–142.

Wilson, D., J. Leon, R. Aster, J. Ni, J. Schlue, S. Grand, S. Semken, S. Baldridge, and W. Gao (2002). Broadband seismic background noise at temporary seismic stations observed on a regional scale in the southwestern United States, *Bull. Seismol. Soc. Am.* **92,** no. 8, 3335–3341, doi: 10.1785/0120010234.

Wolin, E., S. van der Lee, T. A. Bollmann, D. A. Wiens, J. Revenaugh, F. A. Darbyshire, A. W. Frederiksen, S. Stein, and M. E. Wysession (2015). Seasonal and diurnal variations in long-period noise at SPREE stations: The influence of soil characteristics on shallow stations' performance, *Bull. Seismol. Soc. Am.* **105,** no. 5, 2433–2452, doi: 10.1785/0120150046.

Yang, X., G. L. Pavlis, M. W. Hamburger, E. Sherrill, H. Gilbert, S. Marshak, J. Rupp, and T. H. Larson (2014). Seismicity of the Ste. Genevieve seismic zone based on observations from the EarthScope OIINK Flexible Array, *Seismol. Res. Lett.* **85,** no. 6, 1285–1294, doi: 10.1785/0220140079.

Carl Tape
Douglas Christensen
Kyle Smith
Geophysical Institute
University of Alaska Fairbanks
903 Koyukuk Drive
Fairbanks, Alaska 99775 U.S.A.
ctape@alaska.edu

Melissa M. Moore-Driskell
University of North Alabama
Department of Physics and Earth Science
1 Harrison Plaza
Box 5065
Florence, Alabama 35632 U.S.A.

Justin Sweet
IRIS PASSCAL Instrument Center
100 East Road
Socorro, New Mexico 87801 U.S.A.

Published Online 31 May 2017